Uncertainty Propagation for General Stochastic Hybrid Systems on Compact Lie Groups*

Weixin Wang† and Taeyoung Lee†

Abstract. This paper deals with uncertainty propagation of general stochastic hybrid systems (GSHS) where the continuous state space is a compact Lie group. A computational framework is proposed to solve the Fokker-Planck (FP) equation that describes the time evolution of the probability density function for the state of GSHS. The FP equation is split into two parts: the partial differential operator corresponding to the continuous dynamics, and the integral operator arising from the discrete dynamics. These two parts are solved alternatively using the operator splitting technique. Specifically, the partial differential equation is solved by the spectral method where the density function is decomposed into a linear combination of a complete orthonormal function basis brought forth by the Peter-Weyl theorem, thereby resulting an ordinary differential equation. Next, the integral equation is solved by approximating the integral by a finite summation using a quadrature rule. The proposed method is then applied to a three-dimensional rigid body pendulum colliding with a wall, evolving on the product of the three-dimensional special orthogonal group and the Euclidean space. It is illustrated that the proposed method exhibits more accurate numerical results than the conventional Gaussian approach formulated in the tangent space by comparing with a Monte Carlo simulation, while explicitly generating the density function that carries the complete stochastic information of the hybrid state.

Key words. stochastic hybrid system, Fokker-Planck equation, noncommutative harmonic analysis, Lie group

AMS subject classifications. 93C30, 37M05

1. Introduction.

General stochastic hybrid system (GSHS) is a stochastic dynamical system that exhibits both continuous and discrete random behaviors [5]. In a GSHS, the hybrid state consists of two parts: the continuous state that takes the value on a smooth manifold, and the discrete state that lies on a countable set. The continuous dynamics is defined by stochastic differential equations (SDEs) indexed by the discrete state, describing the evolution of continuous state between jumps. The discrete dynamics describes the stochastic jump of the state, which is triggered by a Poisson process with a state-dependent rate function. The uncertainty after the jump is represented by a stochastic kernel. GSHS exhibits rich dynamics caused by the interplay between the continuous state and the discrete counterpart, and it has been used to model various complex systems, such as chemical reactions [12], neuron activities [28], air traffic control [2, 31, 34], and communication networks [11].

Uncertainty propagation involves advecting a probability density along the flow of a dynamical system according to the Fokker–Planck (FP) equation. The probability density can be approximated by, for example, the first n-moments [17], which leads to Monte Carlo methods [10, 27], Gaussian closure methods [13, 22], and equivalent linearization and stochastic averaging [30, 32]. But, Monte Carlo methods do not propagate the probability density func-

*Submitted to the editors DATE.

Funding: This work has been supported in part by AFOSR under the grant FA9550-18-1-0288, and by NSF under the grants CNS-1837382 and CMMI-1760928.

†The George Washington University, DC (wwang442@gwu.edu, tylee@gwu.edu).

tion directly. Other methods involve low-order approximations of the dynamical system, which are suitable only for moderately nonlinear systems as the omitted higher-order terms can lead to significant errors, particularly for long time intervals. For stochastic hybrid systems, uncertainty propagation has been focused on the case when the continuous state lies in the Euclidean space. For example, the interacting multiple model approach [3] and the salted Kalman filter [15] linearize the dynamics and use the Gaussian distribution to describe uncertainties. In [4, 36], particle filters are employed to propagate random samples through the dynamics to approximate the uncertainty distribution. Alternatively, to propagate the probability density function directly, the FP equation has been extended for GSHS into integro-partial differential equations (IPDEs) [1, 11]. And it has been solved using finite difference method [23] and spectral method [38].

In this paper, we study the uncertainty propagation for GSHS whose continuous state evolves on a compact Lie group G. More specifically, given an initial probability distribution of the state, we wish to construct the probability distribution at an arbitrary time through GSHS, by solving the corresponding FP equation represented by IPDEs on G. To address the presence of partial differentiation and integration in the FP equation, we employ the operator splitting method [24]. Specifically, the FP equation is decomposed into two parts: the continuous dynamics which only contains the partial differential operator, and the discrete dynamics which only contains the integral operator. These two individual equations are solved alternatively over a small time step using their respective numerical methods, and they are combined by a first order splitting scheme.

For the partial differential equation corresponding to the continuous dynamics, we use the classic spectral method. The spectral method has been used to solve the FP equations on SE(2) and SO(3) [14, 18, 19, 41, 42] for uncertainty propagation of stochastic dynamical systems without discrete dynamics. It utilizes the Peter-Weyl theorem [29], which states that the matrix components of all finite dimensional irreducible unitary representations of a compact Lie group form a complete orthonormal basis for the space of square integrable functions. As such, an arbitrary probability density function on G can be approximated by a linear combination of the matrix elements of irreducible unitary representations. Further using the operational properties of the representation, the FP equation is transformed into ordinary differential equations (ODEs) of the coefficients, which can be integrated by standard ODE solvers. Next, the integro-differential equation corresponding to the discrete dynamics is approximated by a quadrature rule over a grid, such that the density values on the grid are propagated by another set of ODEs. A useful property is that the grid for the discrete dynamics can be selected to be compatible with the harmonic analysis for the continuous dynamics so as to improve the computational efficiency of the overall splitting scheme.

Compared to conventional methods based on Gaussian distributions formulated in the tangent space of the Lie group [6, 9], the proposed method has the advantage of being non-parametric, i.e., it does not assume a specific family of distributions, but applies to density functions with arbitrary shapes. The proposed method constructs a probability density function, which carries the complete stochastic information about the propagated state, and as such, it can be directly used for visualization or calculating descriptive measures, such as moments, number and locations of local maxima, etc. In this regard, although the Monte Carlo method is also non-parametric, the information of the state is implicitly carried by

random samples, which is usually hard to be distilled into usable forms other than calculating moments, especially when the number of samples is large. Also, the Monte Carlo method cannot deal with large uncertainties efficiently [38]. The downside of the proposed approach is that as a spectral method, its computational complexity increases exponentially with the dimension of continuous space, and quickly becomes infeasible [35].

In short, the main contribution of this paper is the computational framework to propagate uncertainties though GSHS on a compact Lie group. The use of noncommutative harmonic analysis to represent the uncertainty distribution in a global fashion overcomes a fundamental limitation of existing techniques, which implicitly assume that the uncertainty is localized, or has a canonical form. By solving the Fokker–Planck equation directly, the probability density that describes the complete stochastic properties of a hybrid system is propagated.

The rest of this paper is organized as follows: Section 2 reviews the formulation of GSHS considered in this paper, and introduces its associated FP equation. The proposed algorithm for uncertainty propagation is introduced in Section 3 when the continuous state space is a general compact Lie group. In Section 4, we focus on a specific example of a 3D pendulum colliding with a wall, where the continuous state space is $\mathrm{SO}(3) \times \mathbb{R}^2$.

2. Problem Formulation.

In this section, we give a formal definition of the GSHS [5] considered in this paper, and introduce the corresponding FP equation that describes the evolution of the probability density function over time.

2.1. General Stochastic Hybrid System.

The GSHS considered in this paper is defined as a collection $H = \{X, a, b, Init, \lambda, K\}$ as follows:

- $X = G \times S$ is the hybrid state space, where G is a N_g-dimensional compact Lie group, and S is a set composed of N_s discrete modes. The hybrid state is denoted by $(g, s) \in G \times S$.
- $Init : \mathcal{B}(X) \to [0, 1]$ is the initial uncertainty distribution of the hybrid state, where $\mathcal{B}(X)$ is all Borel sets in X.
- The continuous state evolves according to the following stochastic differential equations between discrete jumps:

$$g^{-1}\mathrm{d}g = a(t, g, s)^\wedge \mathrm{d}t + (b(t, s)\mathrm{d}W_t)^\wedge \tag{2.1}$$

  where $a : \mathbb{R} \times X \to \mathbb{R}^{N_g}$ is the drifting vector field, and $b : \mathbb{R} \times S \to \mathbb{R}^{N_g \times N_w}$ is the coefficient matrix for diffusion. Next, W_t is a N_w-dimensional standard Wiener process. The map $(\cdot)^\wedge : \mathbb{R}^{N_g} \to \mathfrak{g}$ is the natural identification of $\mathbb{R}^{N_g}$ and $\mathfrak{g}$, the Lie algebra of G. Since b does not depend on g, (2.1) can be defined either in Ito's or Stratonovich's sense.
- The discrete jump is triggered by a Poisson process, with a rate function $\lambda : X \to \mathbb{R}^+$ dependent on the hybrid state.
- During each discrete jump, the hybrid state is reset according to a stochastic kernel $K : (X, \mathcal{B}(X)) \to [0, 1]$, such that $K(x^-, X^+)$ is the probability of $x^- \in X$ being reset into the set $X^+ \in \mathcal{B}(X)$.

One restriction of the GSHS defined above is that it does not allow the discrete jump to be triggered by the continuous state g entering a certain guard set in a deterministic fashion. However, such *forced* jumps can be approximated by a Poisson process after choosing the rate

function sufficiently large inside the guard set, and zero outside [11]. This will be illustrated by the 3D pendulum example in Section 4.

We also assume the initial distribution has a probability density function for each $s \in S$, i.e., $Init(A) = \sum_{s\in S} \int_{(g,s)\in A} p(t_0, g, s)\mathrm{d}g$ for all $A \in \mathcal{B}(X)$, where $\mathrm{d}g$ is the bi-invariant Haar measure on G normalized such that $\int_{g\in G} \mathrm{d}g = 1$. Furthermore, the discrete transition kernel K can also be written as a set of density functions:

$$K(x^-, X^+) = \sum_{s^+\in S} \int_{(g^+,s^+)\in X^+} \kappa(g^-, s^-, g^+, s^+)\mathrm{d}g^+,$$

where $\kappa : X \times X \to \mathbb{R}$.

Let $(\Omega, \mathcal{F}, \mathbb{P})$ be the underlying probability space, where Ω is the sample space, $\mathcal{F}$ is a sigma-algebra over Ω, and $\mathbb{P}$ denotes the probability measure on $\mathcal{F}$. For a given $\omega \in \Omega$, let $\{u_k(\omega)\}$ be a sequence of independent uniformly distributed random variables on $[0, 1]$. Then an execution of the GSHS defined above can be generated according to the following procedure.

1. Initialize $g(\omega, t_0)$ and $s(\omega, t_0)$ from the initial distribution $Init$.
2. Let $t_1(\omega) = \sup\left\{t \ : \ \exp\left(-\int_{t_0}^{t} \lambda(g(\omega, \tau), s(\omega, t_0))\mathrm{d}\tau\right) > u_1(\omega)\right\}$ be the time of the first jump.
3. During $t \in [t_0, t_1(\omega))$, $g(\omega, t)$ is a sample path of SDE (2.1) with $s = s(\omega, t_0)$, and $s(\omega, t) = s(\omega, t_0)$.
4. At time t_1, the state is reset to $(g(\omega, t_1^+), s(\omega, t_1^+))$ as a sample from the kernel $\kappa(g(\omega, t_1^-), s(\omega, t_0), z^+, s^+)$.
5. If $t_1 < \infty$, repeat from 2) with t_0, s_0, t_1, u_1 replaced by $t_k(\omega)$, $s(\omega, t_k^+)$, $t_{k+1}(\omega)$, $u_{k+1}(\omega)$ for $k = 1, 2, \ldots$.

2.2. Fokker-Planck Equation for GSHS. The FP equation for GSHS describes how its density function evolves over time [1, 7, 11], and it is given as a set of IPDEs as follows:

$$\begin{aligned}\frac{\partial p(t,g,s)}{\partial t} =& \underbrace{-\sum_{i=1}^{N_g} \mathfrak{d}_j \left(a_j(t,g,s)p(t,g,s)\right) + \sum_{j,k=1}^{N_g} D_{j,k}(t,s)\mathfrak{d}_j\mathfrak{d}_k p(t,g,s)}_{\mathcal{L}_c^* p(t,g,s)} \\ &+ \underbrace{\sum_{s^-\in S} \int_{g^-\in G} \kappa(g^-, s^-, g, s)\lambda(g^-, s^-)p(t, g^-, s^-)\mathrm{d}g^- - \lambda(g, s)p(t, g, s)}_{\mathcal{L}_d^* p(t,g,s)},\end{aligned} \tag{2.2}$$

where the subscripts denote the indices of a vector or matrix, and $D = \frac{1}{2}bb^T$. Moreover, $\mathfrak{d}_j$ is the left-trivialized derivative of a function on G, i.e., $\mathfrak{d}_j f(g) = \frac{\mathrm{d}}{\mathrm{d}t}\big|_{t=0} f\big(g\exp(t\hat{e}_j)\big)$, where $\exp : \mathfrak{g} \to G$ is the exponential map, and e_j is the j-th standard base vector of $\mathbb{R}^{N_g}$. For each $s \in S$, (2.2) defines an IPDE for $p(t, g, s)$, and thus, there are a total of N_s IPDEs.

The FP equation can be interpreted as follows. The first two terms on the right hand side of (2.2) represent the evolution caused by the continuous process: the first one represents advection due to the drift vector field, and the second corresponds to diffusion caused by

noise, or the Wiener process. The last two terms of (2.2) describe the evolution due to discrete jumps. The third term represents the densities transitioned into (g, s) from (g^-, s^-) before the jump, weighted by how likely the jump happens (λ), and how likely the density is transitioned into (g, s) (κ). The last term represents the density transitioned out of (g, s). To distinguish these two parts explicitly, (2.2) is written as

$$\frac{\partial p(t,g,s)}{\partial t} = \mathcal{L}_c^* p(t,g,s) + \mathcal{L}_d^* p(t,g,s), \tag{2.3}$$

where $\mathcal{L}_c^*$ and $\mathcal{L}_d^*$ denote the adjoint of the infinitesimal generators of the continuous SDE, and the discrete jump of the GSHS, respectively.

The FP equation (2.2) describes the evolution of the probability density along the flows of GSHS on a Lie group. In contrast to the Fokker–Planck equation of non-hybrid systems, which is a partial-differential equation, (2.2) exhibits fundamental challenges, as it is an *integro-partial differential equation* that involves both partial differentiation and integration. Another challenge is that the probability density is defined on a nonlinear Lie group G, so the existing computational techniques in solving the Fokker–Planck equation on a linear space $\mathbb{R}^n$ cannot be directly applied. In this paper, these are addressed by utilizing noncommutative harmonic analysis and the splitting technique.

3. Uncertainty Propagation for GSHS.

In this section, we present a computational framework to solve (2.3) via the spectral method using noncommutative harmonic analysis on G. However, the integral term in (2.2) causes issues in the spectral method as there is no closed formula to express the Fourier coefficients of the integral of a function $f(g)$ over G as the Fourier coefficients of f. Even though a closed formula exists on $\mathbb{R}^N$, it has been shown that taking the Fourier transform of the integral term directly involves intensive computations [39].

Instead, we adopt the operator splitting technique, where (2.3) is split into two equations:

$$\frac{\partial p^c(t,g,s)}{\partial t} = \mathcal{L}_c^* p^c(t,g,s), \tag{3.1a}$$

$$\frac{\partial p^d(t,g,s)}{\partial t} = \mathcal{L}_d^* p^d(t,g,s). \tag{3.1b}$$

The desirable features are that in the absence of the term $\mathcal{L}_d^* p$, (3.1a) corresponds to a PDE on G for each discrete state; and without $\mathcal{L}_c^* p$, (3.1b) becomes an integro-differential equation without partial differentiation. These can be addressed by using the spectral method and numerical quadrature respectively. Then, the solution of each part can be combined with the operator splitting.

3.1. Propagation over Continuous Dynamics.

First, we solve (3.1a) via noncommutative harmonic analysis. The objective is to decompose the density function $p^c(t, g, s)$ into a linear combination of an orthonormal basis of a function space on G for each $t \geq t_0$ and $s \in S$. Then (3.1a) can be converted to a set of ODEs for the coefficients of the linear combination, which can be solved via standard numerical integration schemes for ODE.

We first summarize harmonic analysis on a compact Lie group G [8, 26]. Let $U^l(g) : G \to \mathrm{GL}(d(l), \mathbb{C})$ be the l-th irreducible unitary representation of G with a finite dimension $d(l)$, and the collection of all l be denoted by $\hat{G}$. Then by the Peter-Weyl theorem, the functions $\left\{\{U^l_{m_1,m_2}\}_{m_1,m_2=1}^{d(l)}\right\}_{l\in\hat{G}}$ form an orthonormal basis of the function space $L^2(G)$. That is, for any square integrable function $f : G \to \mathbb{C}$, it can be decomposed as a linear combination

$$f(g) = \sum_{l\in\hat{G}} \sum_{m_1,m_2=1}^{d(l)} d(l)\mathcal{F}^l_{m_1,m_2}[f]U^l_{m_1,m_2}(g), \tag{3.2}$$

where $\mathcal{F}^l_{m_1,m_2}[f]$ are the Fourier coefficients of f, given by the (m_1, m_2)-th entry of

$$\mathcal{F}^l[f] = \int_{g\in G} f(g)U^l(g^{-1})^T \mathrm{d}g = \int_{g\in G} f(g)\overline{U^l(g)}\mathrm{d}g. \tag{3.3}$$

Equation (3.2) and (3.3) are called the inverse and forward Fourier transform of function f.

One crucial property is that we can express the Fourier coefficient of the derivative $\mathcal{F}[\mathfrak{d}_j f]$ in terms of $\mathcal{F}[f]$ [8]. Let $u^l : \mathfrak{g} \to \mathfrak{gl}(d(l), \mathbb{C})$ be the associated Lie algebra representation of U^l, i.e., for all $X \in \mathfrak{g}$, $u^l(X) = \frac{\mathrm{d}}{\mathrm{d}t}\big|_{t=0} U^l(\exp(tX))$. Then, we have

$$\mathcal{F}^l[\mathfrak{d}_j f] = \mathcal{F}^l[f]u^l(\hat{e}_j)^T. \tag{3.4}$$

It should be noted in some other works, the subscripts for $F^l_{m1,m2}[f]$ are reversed relative to $F^l_{m2,m1}[f]$ in (3.2). Under this convention, (3.3) and (3.4) should be modified accordingly (see for example Section 8.3 in [8]).

Using these, (3.1a) can be transformed into a set of ODEs for the Fourier coefficients of $p^c(t, g, s)$ as follows.

Theorem 3.1. *Let $\mathcal{F}[p^c](t, s)$ be the Fourier coefficients of $p^c(t, g, s)$ which depend on t and s. For any $s \in S$, if $p^c(t, g, s)$ satisfies (3.1a), then $\mathcal{F}[p^c](t, s)$ approximately satisfies the following ODE:*

$$\frac{\mathrm{d}}{\mathrm{d}t}\mathcal{F}^l[p^c](t, s) = -\sum_{j=1}^{N_g} \mathcal{F}^l[a_j p^c](t, s)u^l(\hat{e}_j)^T + \sum_{j,k=1}^{N_g} D_{j,k}\mathcal{F}^l[p^c](t, s)u^l(\hat{e}_k)^T u^l(\hat{e}_j)^T. \tag{3.5}$$

Proof. Suppose $p^c(t, g, s)$ is approximated by a band-limited [26] sum of its Fourier series:

$$p^c(t, g, s) \approx \sum_{l\in\hat{G}_0} \sum_{m_1,m_2=1}^{d(l)} d(l)\mathcal{F}^l_{m_1,m_2}[p^c](t, s)U^l_{m_1,m_2}(g), \tag{3.6}$$

where $\hat{G}_0$ is a finite subset of $\hat{G}$. Substitute the above equation and a similar band-limited expansion of $\mathcal{L}^*_c p^c$ into (3.1a), we get for all $s \in S$

$$\sum_{l\in\hat{G}_0} \sum_{m_1,m_2=1}^{d(l)} d(l)\frac{\mathrm{d}}{\mathrm{d}t}\mathcal{F}^l_{m_1,m_2}[p^c](t, s)U^l_{m_1,m_2}(g) \approx \sum_{l\in\hat{G}_0} \sum_{m_1,m_2=1}^{d(l)} d(l)\mathcal{F}^l_{m_1,m_2}[\mathcal{L}^*_c p^c](t, s)U^l_{m_1,m_2}(g).$$

Due to the orthogonality of basis, we can equate the Fourier coefficient with the same indices, i.e. $\frac{\mathrm{d}}{\mathrm{d}t}\mathcal{F}^l_{m_1,m_2}[p^c](t,s) = \mathcal{F}^l_{m_1,m_2}[\mathcal{L}^* p^c](t,s)$ for any $s \in S$. Equation (3.5) can be derived by expanding $\mathcal{L}^* p^c$ using the differentiation formula (3.4). ∎

Equation (3.5) is ODEs of the Fourier coefficients $\mathcal{F}^l_{m_1,m_2}[p^c](t,s)$, and can be integrated using numerical ODE solvers. To illustrate how the calculations can be carried out in practice, we present with the simplest forward Euler's method. Suppose a grid $\{g_\nu\}_{\nu=1}^{N_q}$ is put onto G, and there is a quadrature rule $\{w_\nu\}_{\nu=1}^{N_q}$ such that the integral in (3.3) can be approximated by a finite summation:

$$\mathcal{F}^l[f] = \sum_{\nu=1}^{N_q} w_\nu f(g_\nu)\overline{U^l(g_\nu)}. \tag{3.7}$$

This allows the forward Fourier transform to be computed. Suppose at time $t = t_k$, the values of $p^c(t_k, g_\nu, s)$, $a(t_k, g_\nu, s)$ on the grid, and $D(t_k, s)$ are given. Then the Fourier coefficients $\mathcal{F}^l[a_j p^c](t_k, s)$, and $\mathcal{F}^l[p^c](t_k, s)$ for $l \in \hat{G}_0$ can be calculated as in (3.7) using the quadrature rule. Namely, the right hand side of (3.5), i.e., $\mathcal{F}^l[\mathcal{L}_c^* p^c](t_k, s)$ can be calculated, which enables the first order integration $\mathcal{F}^l[p^c](t_{k+1}, s) = \mathcal{F}^l[p^c](t_k, s) + \mathcal{F}^l[\mathcal{L}_c^* p^c](t_k, s)\Delta t$. And the values of $p^c(t_{k+1}, g_\nu, s)$ on the grid can be recovered by (3.6), which can be used in the next integration step. The pseudocode is summarized in Algorithm 3.1, where the first order integration can easily be replaced by other higher order numerical integration schemes.

The summations in (3.7) and (3.6) can be accelerated using extensions of the classic Cooley-Tukey FFT algorithm to compact Lie groups. See for example [33] for a review on this topic. The FFT algorithms have been developed for classic compact matrix Lie groups $\mathrm{SO}(n)$, $\mathrm{U}(n)$, $\mathrm{SU}(n)$ and $\mathrm{Sp}(n)$ in [26].

3.2. Propagation over Discrete Dynamics. Next, consider (3.1b). We apply the quadrature rule on G to the integral term on the right hand side of (3.1b), where the integration over G is replaced by a finite summation over the grid:

$$\frac{\mathrm{d}p^d(t, g_\nu, s)}{\mathrm{d}t} = \sum_{s^- \in S} \sum_{\nu'=1}^{N_q} w_{\nu'} \kappa(g^-_{\nu'}, s^-, g_\nu, s)\lambda(g^-_{\nu'}, s^-)p^d(t, g^-_{\nu'}, s^-) - \lambda(g_\nu, s)p^d(t, g_\nu, s), \tag{3.8}$$

where g_ν and g'_ν are lattices of the grid on G. The above is a set of linear ODEs of $p^d(t, g_\nu, s)$ with $N_s \cdot N_q$ equations. Suppose at time $t = t_k$, the values of $p^d(t_k, g_\nu, s)$ on the grid are given, then the values of p^d at time $t = t_{k+1}$ can be integrated using the forward Euler's method as $p(t_{k+1}, g_\nu, s) = p(t_k, g_\nu, s) + \mathcal{L}_d^* p^d(t_k, g_\nu, s)\Delta t$, where $\mathcal{L}_d^* p^d(t_k, g_\nu, s)$ is calculated as the right hand side of (3.8). The pseudocode is summarized in Algorithm 3.1.

3.3. Splitting Method. In summary, (3.1a) is transformed into ODEs of Fourier coefficients, and (3.1b) is converted into ODEs of probability densities on the grid. The numerical solutions of these two equations are combined using a first order splitting scheme as follows. Suppose the time is discretized by a sequence $\{t_k\}_{k=0}^{\infty}$ with a fixed increment $\Delta t = t_{k+1} - t_k$. Given $p(t_k, g, s)$, we first solve (3.1a) with the initial condition $p^c(t_k, g, s) = p(t_k, g, s)$ to obtain $p^c(t_{k+1}, g, s)$ that is propagated over the continuous dynamics. Next, we solve (3.1b) with

the initial condition $p^d(t_k, g, s) = p^c(t_{k+1}, g, s)$ to propagate it over the discrete dynamics, and construct $p^d(t_{k+1}, g, s)$ which is taken as the solution of (2.2) at t_{k+1}. These two parts are integrated seamlessly, as the probability density values propagated over the discrete dynamics are on the grid designed for the Fourier transform required for the propagation over the continuous dynamics. The pseudocode is summarized in Algorithm 3.1.

Algorithm 3.1 Uncertainty propagation for GSHS

procedure $p(t_{k+1}, g_\nu, s) =$ UNCERTAINTY_PROPAGATION$(p(t_k, g_\nu, s))$
  $p^c(t_k, g_\nu, s) = p(t_k, g_\nu, s)$.
  $p^c(t_{k+1}, g_\nu, s) =$ PROPAGATE_CONTINUOUS$(p^c(t_k, g_\nu, s))$.
  $p^d(t_k, g_\nu, s) = p^c(t_{k+1}, g_\nu, s)$.
  $p^d(t_{k+1}, g_\nu, s) =$ PROPAGATE_DISCRETE$(p^d(t_k, g_\nu, s))$.
  $p(t_{k+1}, g_\nu, s) = p^d(t_{k+1}, g_\nu, s)$.
end procedure

procedure $p^c(t_{k+1}, g_\nu, s) =$ PROPAGATE_CONTINUOUS$(p^c(t_k, g_\nu, s))$
  for $s \in S$ **do**
    for $l \in \hat{G}_0$ **do**
      for $j = 1, \ldots, N_g$ **do**
        Compute $\mathcal{F}^l[a_j p^c](t_k, s)$ using (3.7).
      end for
      Compute $\mathcal{F}^l[p^c](t_k, s)$ using (3.7).
      Compute $\mathcal{F}^l(\mathcal{L}_c^* p^c)(t_k, s)$ using the right hand side of (3.5).
      $\mathcal{F}^l[p^c](t_{k+1}, s) = \mathcal{F}^l[p^c](t_k, s) + \mathcal{F}^l(\mathcal{L}_c^* p^c)(t_k, s)\Delta t$.
    end for
    Recover $p^c(t_{k+1}, g_\nu, s)$ from $\mathcal{F}^l[p^c](t_{k+1}, s)$ using (3.6).
  end for
end procedure

procedure $p^d(t_{k+1}, g_\nu, s) =$ PROPAGATE_DISCRETE$(p^d(t_k, g_\nu, s))$
  for $s \in S$ and $\nu = 1, \ldots, N_q$ **do**
    Compute $\mathcal{L}_d^* p^d(t_k, g_\nu, s)$ using the right hand side of (3.8).
    $p^d(t_{k+1}, g_\nu, s) = p^d(t_k, g_\nu, s) + \mathcal{L}_d^* p^d(t_k, g_\nu, s)\Delta t$.
  end for
end procedure

4. Numerical Example of 3D Pendulum.

A 3D pendulum is a rigid body that freely rotates about an inertially-fixed pivot under gravity. In this section, we apply the proposed method to the 3D pendulum model, to propagate the uncertainties of its attitude and angular velocity. For the discrete dynamics, we assume that the 3D pendulum may collide with a fixed planar wall, which causes an instantaneous change of its angular velocity (see Figure 4.1).

4.1. 3D Pendulum Model.

We use the GSHS defined in Section 2.1 to model the 3D pendulum as follows. Two reference frames are used: the inertial frame $\{\vec{e}_1, \vec{e}_2, \vec{e}_3\}$, and the body-fixed frame of the pendulum $\{\vec{b}_1, \vec{b}_2, \vec{b}_3\}$. The origin of the body-fixed frame is at the

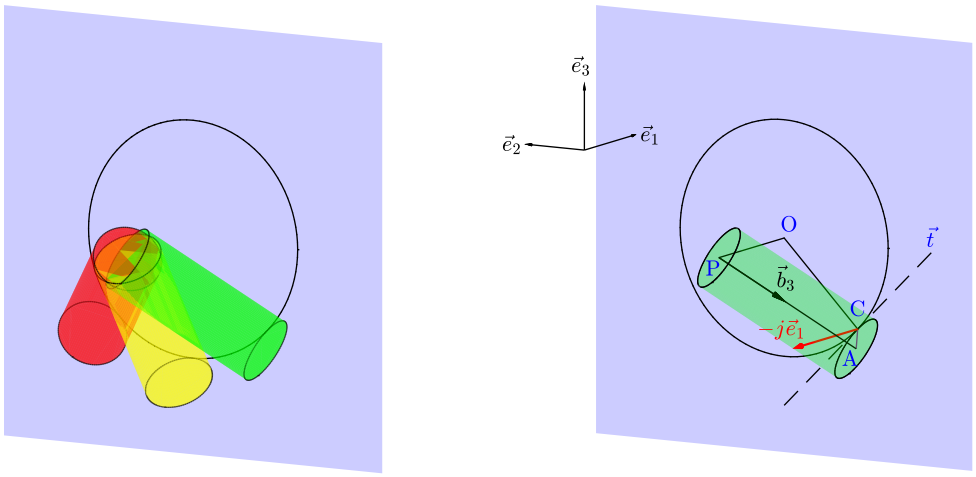

(a) Possible collision configurations.

(b) Collision response.

Figure 4.1: An Axially symmetric 3D pendulum colliding with a wall.

pivot point denoted by P. The continuous state is $(R, \Omega) \in G = \mathrm{SO}(3) \times \mathbb{R}^3$, where $R \in \mathrm{SO}(3)$ is the attitude of the pendulum, i.e., the linear transform of coordinates from the body-fixed frame to the inertial frame, and $\Omega \in \mathbb{R}^3$ is the coordinates of angular velocity in the body-fixed frame. The discrete state space is $S = \{1\}$, i.e., there is only one discrete mode. Throughout this section, for any vector $\vec{a}$, $a \in \mathbb{R}^3$ denotes its coordinates in the inertial frame, if not stated otherwise.

Continuous Dynamics. The continuous dynamics is given by the following SDE:

$$R^T \mathrm{d}R = \hat{\Omega} \mathrm{d}t, \tag{4.1a}$$

$$\mathrm{d}\Omega = \left(J^{-1}(-\Omega \times J\Omega - mg\rho \times R^T e_3) - B\Omega\right) \mathrm{d}t + H_c \mathrm{d}W_t, \tag{4.1b}$$

where $J \in \mathbb{R}^{3\times3}$ is the moment of inertia about the pivot, and $m \in \mathbb{R}$ is the mass. The coordinates of the center of mass are given by $\rho \in \mathbb{R}^3$ in the body-fixed frame. The fixed gravitational acceleration is denoted by $g \in \mathbb{R}$. There is a damping torque proportional to the angular velocity scaled by the matrix $B = \mathrm{diag}(B_1, B_2, B_3) \in \mathbb{R}^{3\times3}$. Finally, $W_t \in \mathbb{R}^3$ is the standard Wiener process, representing random external torques.

We make the following assumptions to simplify the continuous dynamics: (i) the pendulum is axially symmetric, i.e., $J = \mathrm{diag}(J_1, J_1, J_3)$, and $\rho = [0, 0, \rho_z]^T$ is along the axis $\vec{b}_3$; (ii) $Init(\{\Omega_3 = 0\}) = 1$, i.e., the initial angular velocity along the axis of symmetry is zero with probability one; (iii) the third row of H_c is zero. Under these assumptions, it is straightforward to verify that $\mathbb{P}(\Omega_3(t) = 0) = 1$ for any $t > t_0$. As a consequence, we may ignore Ω_3 and

reduce the continuous state space into $G = \mathrm{SO}(3) \times \mathbb{R}^2$. The resulting SDE is given by

$$R^T \mathrm{d}R = \left(\begin{bmatrix} \tilde{\Omega}^T & 0 \end{bmatrix}^T \right)^\wedge \mathrm{d}t, \tag{4.2a}$$

$$\mathrm{d}\tilde{\Omega} = \left(\frac{mg\rho_z}{J_1} \begin{bmatrix} R_{32} \\ -R_{31} \end{bmatrix} - \tilde{B}\tilde{\Omega} \right) \mathrm{d}t + \tilde{H}_c \mathrm{d}W_t, \tag{4.2b}$$

where $\tilde{\Omega} = [\Omega_1, \Omega_2]^T$, $\tilde{B} = \mathrm{diag}(B_1, B_2)$, and $\tilde{H}_c$ is the first two rows of H_c.

Discrete Dynamics. A planar wall is placed perpendicular to the inertial $\vec{e}_1$ axis, at $d_{\text{wall}} > 0$ from the pivot point P. As the pendulum swings, it may collide with the wall and rebound. We further assume the pendulum is a cylinder with the height h and the radius r. Then, all possible collision points between the pendulum and the wall form a circle, as illustrated in Figure 4.1a. Let the angle between the $\vec{e}_1$-$\vec{e}_2$ plane and $\vec{b}_3$ be denoted by $\theta = \arcsin(\vec{b}_3 \cdot \vec{e}_1)$. A collision occurs when

$$\theta \geq \theta_0 = \arcsin \frac{d_{\text{wall}}}{\sqrt{h^2 + r^2}} - \arcsin \frac{r}{\sqrt{h^2 + r^2}}, \tag{4.3a}$$

$$(R\Omega \times \varrho) \cdot e_1 > 0, \tag{4.3b}$$

where $\varrho \in \mathbb{R}^3$ is the coordinates of the vector $\overrightarrow{PC} = (h - r\tan\theta)\vec{b}_3 + r\sec\theta\vec{e}_1$ in the inertial frame, and C is the point on the pendulum that has the largest coordinate along $\vec{e}_1$.

The first equation states that the pendulum penetrates through the wall, and the second equation implies that the pendulum is rotating towards the wall. Equation (4.3) represents a guard set defined such that whenever the continuous state enters it, the discrete jump is triggered. This corresponds to a deterministic forced jump of hybrid systems. In the presented GSHS, a Poisson process can be designed to approximate this forced jump, with a rate function $\lambda(R, \Omega)$ being very large when (4.3) is satisfied, and zero otherwise. However, one must make a compromise on the space variation of λ. Specifically, the ideal λ would make the probability density p^c large outside the guard set, and close to zero inside, i.e., there is a large space variation of p^c caused by the discontinuity at the boundary. This is unfavorable for the spectral method, since a high bandwidth must be used to capture the large space variation, at the cost of increased computational load. Here we design a rate function corresponding to (4.3) with a relatively small space variation as

$$\lambda(R, \Omega) = \begin{cases} \frac{\lambda_{\max}}{2} \sin\left(\frac{pi}{2\theta_t}(\theta - \theta_0) \right) + \frac{\lambda_{\max}}{2}, & \text{if } -\theta_t \leq \theta - \theta_0 \leq \theta_t,\ R\Omega \times \varrho \cdot e_1 > 0 \\ \lambda_{\max}, & \text{if } \theta - \theta_0 > \theta_t,\ R\Omega \times \varrho \cdot e_1 > 0 \\ 0, & \text{otherwise} \end{cases}. \tag{4.4}$$

Namely, a threshold $\theta_t > 0$ is used to mark a "boundary region" of the guard set, and the sine function is used to make a smooth connection between the large $\lambda_{\max} > 0$ inside the guard set, and zero outside (Figure 4.2).

Next, we formulate the stochastic kernel describing the state distribution immediately after a jump. During the collision, an impulse $-j\vec{e}_i$ with $j > 0$ is applied to the pendulum at the collision point C (Figure 4.1b) that redirects the linear velocity of the pendulum at C

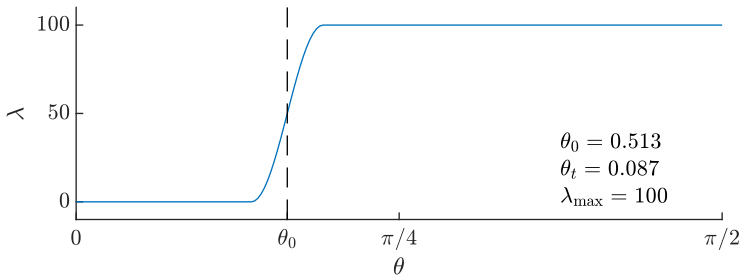

Figure 4.2: $\lambda(R, \Omega)$ versus $\theta(R)$ when $(R\Omega \times \varrho) \cdot e_1 > 0$.

along $\vec{e}_1$. First assume there is no noise, then the collision response can be summarized in terms of the change of angular velocity and linear velocity at C, as follows:

$$\bar{\Omega}^+ - \Omega^- = J^{-1} R^T (\varrho \times (-j e_1)), \tag{4.5a}$$

$$(R\bar{\Omega}^+ \times \varrho) \cdot e_1 = -\varepsilon (R\Omega^- \times \varrho) \cdot e_1, \tag{4.5b}$$

where Ω^-, $\bar{\Omega}^+$ denote the angular velocities before and after collision respectively, and $0 < \varepsilon \leq 1$ is the coefficient of restitution. Note that $t \triangleq (\varrho \times e_1)/|\varrho \times e_1|$ is perpendicular to b_3, since $J = \mathrm{diag}(J_1, J_1, J_3)$, it can be verified that $J^{-1} R^T t = \frac{1}{J_1} R^T t$. This indicates that $\bar{\Omega}^+ - \Omega^-$ is along $R^T t$ and is perpendicular to $R^T b_3$, thus $\bar{\Omega}_3^+ = \Omega_3^-$ and we may ignore Ω_3 as we did in the continuous dynamics where $\mathbb{P}(\Omega_3 = 0) = 1$. Furthermore, (4.5b) can be simplified into

$$\bar{\Omega}^+ = \Omega^- - (1 + \varepsilon)(\Omega^- \cdot R^T t) R^T t, \tag{4.6}$$

which gives the continuous state Ω right after the collision in an ideal case. Here we further assume that the angular velocity is also perturbed by a Gaussian noise during collision, i.e.,

$$\Omega^+ = \bar{\Omega}^+ + \begin{bmatrix} H_d \xi \\ 0 \end{bmatrix}, \tag{4.7}$$

where Ω^+ is the perturbed angular velocity after collision, $H_d \in \mathbb{R}^{2\times 2}$, and ξ is a 2-dimensional standard Gaussian random vector.

In short, the stochastic kernel for discrete jump caused by the collision can be written as

$$\begin{aligned} \kappa(R^-, \tilde{\Omega}^-, R^+, \tilde{\Omega}^+) =& \delta_{\mathrm{SO(3)}} \left(R^+ (R^-)^T \right) \\ & \times \frac{1}{2\pi \sqrt{\det \Sigma_d}} \exp \left\{ -\tfrac{1}{2} \left(\tilde{\Omega}^+ - \tilde{\bar{\Omega}}_0^+ \right)^T \Sigma_d^{-1} \left(\tilde{\Omega}^+ - \tilde{\bar{\Omega}}_0^+ \right) \right\}, \end{aligned} \tag{4.8}$$

where $\Sigma_d = H_d H_d^T$, and $\delta_{\mathrm{SO(3)}}$ is the Dirac-delta function on SO(3). In other words, the discrete jump does not alter the attitude R, while it resets the angular velocity from $\tilde{\Omega}^-$ to $\tilde{\bar{\Omega}}^+$ with Gaussian distributed random noises.

4.2. Harmonic Analysis on $\mathrm{SO}(3)\times\mathrm{T}^2$. One obstacle in applying the proposed approach to the pendulum model is that the continuous state space, namely $\mathrm{SO}(3)\times\mathbb{R}^2$ is not compact. Nevertheless, since the angular velocity is uniformly bounded by the initial mechanical energy of the pendulum, as long as $p(t_0, R, \tilde{\Omega})$ is compactly supported, we may assume $p(t, R, \tilde{\Omega})$ is compactly supported, uniformly in time t. Therefore, the continuous state space can be regarded as $\mathrm{SO}(3)\times\mathrm{T}^2$, where $\mathrm{T}^2 = \mathrm{S}^1\times\mathrm{S}^1$ is the 2-dimensional torus. Noncommutative harmonic analysis on $\mathrm{SO}(3)$ has been presented in [8, 37], and harmonic analysis on S is widely available. Here we review those materials needed to formulate harmonic analysis on $\mathrm{SO}(3)\times\mathrm{T}^2$.

Representation. Let the representations of $\mathrm{SO}(3)$ be denoted by $\{U^l(R)\}_{l\in\mathbb{N}}$, where the dimension of $U^l(R)$ is $d(l) = 2l+1$. Suppose that $R\in\mathrm{SO}(3)$ is parameterized by the 3-2-3 Euler angles as

$$R(\alpha,\beta,\gamma) = \exp(\alpha\hat{e}_3)\exp(\beta\hat{e}_2)\exp(\gamma\hat{e}_3), \tag{4.9}$$

where $\alpha,\gamma\in[0,2\pi)$, $\beta\in[0,\pi]$. For $-l\le m_1,m_2\le l$, the elements of the l-th representation $U^l(R)$ can be explicitly written as

$$U^l_{m_1,m_2}(R(\alpha,\beta,\gamma)) = e^{-im_1\alpha}d^l_{m_1,m_2}(\beta)e^{-im_2\gamma}, \tag{4.10}$$

where $d^l_{m_1,m_2}(\beta)$ is the real valued Wigner-d function [37]. Next, the representations of T^2 are given by

$$V^n(\tilde{\Omega}) = \exp\left(\frac{i\pi n_1\Omega_1}{L} + \frac{i\pi n_2\Omega_2}{L}\right) \tag{4.11}$$

for $n = (n_1, n_2)\in\mathbb{Z}^2$, where (Ω_1,Ω_2) is normalized by its uniform bound $L>0$, such that $\pi\Omega_j/L\in[-\pi,\pi)$, $j=1,2$, so $\tilde{\Omega}\in\mathrm{T}^2$. Then, the representations of $\mathrm{SO}(3)\times\mathrm{T}^2$ are given by the tensor product of U^l and V^n, and more explicitly $\{\{U^l_{m_1,m_2}(R)\cdot V^n(\tilde{\Omega})\}^l_{m_1,m_2=-l}\}_{l\in\mathbb{N},n\in\mathbb{Z}^2}$, which forms a complete orthonormal basis for the function space $L^2(\mathrm{SO}(3)\times\mathrm{T}^2)$.

Sampling Theorem. Consider a band-limited function on $\mathrm{SO}(3)\times\mathrm{T}^2$ spanned by the representations with $l\le l_0-1$ and $-n_0\le n_1,n_2\le n_0-1$. According to the sampling theorem, its Fourier coefficients can be exactly recovered by the sample values on a certain grid and the associated quadrature rule. The grid on $\mathrm{SO}(3)$ can be designed in terms of Euler angles, with $2l_0$ points along each dimension:

$$\alpha_{\nu_1} = \frac{\pi\nu_1}{l_0},\qquad \beta_{\nu_2} = \frac{\pi(2\nu_2+1)}{4l_0},\qquad \gamma_{\nu_3} = \frac{\pi\nu_3}{l_0}, \tag{4.12}$$

for $\nu_1,\nu_2,\nu_3 = 0,\dots,2l_0-1$. The quadrature rule associated with this grid [16] is

$$w_\nu = \frac{1}{4l_0^3}\sin(\beta_{\nu_2})\sum_{j=0}^{l_0-1}\frac{1}{2j+1}\sin((2j+1)\beta_{\nu_2}). \tag{4.13}$$

Similarly, a grid on T^2 can be defined as

$$\frac{\pi(\Omega_1)_{\mu_1}}{L} = \frac{\mu_1\pi}{n_0},\qquad \frac{\pi(\Omega_2)_{\mu_2}}{L} = \frac{\mu_2\pi}{n_0}, \tag{4.14}$$

for $\mu_1, \mu_2 = -n_0, \ldots, n_0 - 1$. The quadrature rule is simply

$$w_\mu = \frac{1}{(2n_0)^2}. \tag{4.15}$$

Using the above orthonormal basis and quadrature rules, the forward Fourier transform (3.3) can be computed using the following finite summation:

$$\begin{aligned}\mathcal{F}^{l,n}_{m_1,m_2}[f] = &\sum_{\mu_1,\mu_2=-n_0}^{n_0-1} \sum_{\nu_1,\nu_2,\nu_3=0}^{2l_0-1} w_\nu w_\mu f\Big(R(\alpha_{\nu_1}, \beta_{\nu_2}, \gamma_{\nu_3}), (\Omega_1)_{\mu_1}, (\Omega_2)_{\mu_2}\Big) \\ &\cdot e^{im_1\alpha_{\nu_1}} d^l_{m_1,m_2}(\beta_{\nu_2}) e^{im_2\gamma_{\nu_3}} \cdot \exp\left(-\frac{in_1\pi(\Omega_1)_{\mu_1}}{L} - \frac{in_2\pi(\Omega_2)_{\mu_2}}{L}\right),\end{aligned} \tag{4.16}$$

for any $0 \le l \le l_0 - 1$, $-l \le m_1, m_2 \le l$, and $-n_0 \le n_1, n_2 \le n_0 - 1$. Conversely, the backward Fourier transform (3.6) can be explicitly written as

$$\begin{aligned}f\Big(R(\alpha_{\nu_1}, \beta_{\nu_2}, \gamma_{\nu_3}), (\Omega_1)_{\mu_1}, (\Omega_2)_{\mu_2}\Big) = &\sum_{n_1,n_2=-n_0}^{n_0-1} \sum_{l=0}^{l_0-1} \sum_{m_1,m_2=-l}^{l} (2l+1)\mathcal{F}^{l,n}_{m_1,m_2}[f] \\ &\cdot e^{-im_1\alpha_{\nu_1}} d^l_{m_1,m_2}(\beta_{\nu_2}) e^{-im_2\gamma_{\nu_3}} \cdot \exp\left(\frac{in_1\pi(\Omega_1)_{\mu_1}}{L} + \frac{in_2\pi(\Omega_2)_{\mu_2}}{L}\right),\end{aligned} \tag{4.17}$$

to recover the function values on the grid. The summations in (4.16) and (4.17) can be computed using a combination of the classic Cooley-Tukey FFT algorithm, and the FFT developed specifically for SO(3) [16].

4.3. Implementation. Now, the proposed method is implemented to the pendulum model as follows.

Continuous Dynamics. First, for the continuous dynamics (4.2), the corresponding FP equation (3.1a) can be written as

$$\begin{aligned}\frac{\partial p^c(t,R,\tilde{\Omega})}{\partial t} = &-\sum_{j=1}^{2} \mathfrak{d}_j\big(\Omega_j p^c(t,R,\tilde{\Omega})\big) - \sum_{j=1}^{2} \frac{\partial}{\partial \Omega_j}\big(a^g_j(R) p^c(t,R,\tilde{\Omega})\big) \\ &+ \sum_{j=1}^{2} B_j \frac{\partial}{\partial \Omega_j}\big(\Omega_j p^c(t,R,\tilde{\Omega})\big) + \sum_{j,k=1}^{2} \tilde{D}_{jk} \frac{\partial}{\partial \Omega_j \partial \Omega_k} p^c(t,R,\tilde{\Omega}),\end{aligned} \tag{4.18}$$

where $a^g(R) = \frac{mg\rho_z}{J_1}[R_{32}, -R_{31}]^T$, and $\tilde{D} = \frac{1}{2}\tilde{H}_c\tilde{H}_c^T$. Next, we present selected operational properties of the representations that are required to perform the Fourier transform for the right hand side of the above expression. For the representation $U^l(R)$ of SO(3), the associated Lie algebra representation has explicit forms:

$$u^l_{m_1,m_2}(\hat{e}_1) = -\tfrac{1}{2}ic^l_{m_2}\delta_{m_1-1,m_2} - \tfrac{1}{2}ic^l_{-m_2}\delta_{m_1+1,m_2}, \tag{4.19a}$$

$$u^l_{m_1,m_2}(\hat{e}_2) = -\tfrac{1}{2}c^l_{m_2}\delta_{m_1-1,m_2} + \tfrac{1}{2}c^l_{-m_2}\delta_{m_1+1,m_2}, \tag{4.19b}$$

$$u^l_{m_1,m_2}(\hat{e}_3) = -im_1\delta_{m_1,m_2}, \tag{4.19c}$$

where $c_m^l = \sqrt{(l-m)(l+m+1)}$. These can be used to calculate $\mathcal{F}^{l,n}[\mathfrak{d}_j(\Omega_j p^c)]$, the first term on the right hand side of (4.18), as in (3.4). Also, the Lie algebra representation associated with $V^n(\tilde{\Omega})$ is

$$v^n(e_j) = \frac{i\pi n_j}{L}, \qquad j = 1, 2, \tag{4.20}$$

which can be used to obtain those terms involving $\mathcal{F}^{l,n}[\frac{\partial}{\partial \Omega_j}]$ and $\mathcal{F}^{l,n}[\frac{\partial^2 p^c}{\partial \Omega_j \partial \Omega_k}]$ in (4.18). Furthermore, utilizing the inverse convolution theorem specific to the Fourier series on T^N, for any $f \in L^2(\mathrm{SO}(3) \times \mathrm{T}^2)$ and $g \in L^2(\mathrm{T}^2)$, we may calculate the Fourier coefficient of $f \cdot g$ directly from those of f and g:

$$\mathcal{F}^{l,n}_{m_1,m_2}[fg] = \sum_{n_1', n_2' = -n_0}^{n_0 - 1} \mathcal{F}^{l,n-n'}_{m_1,m_2}[f] \mathcal{F}^{n'}[g], \tag{4.21}$$

where $n - n' = (n_1 - n_1', n_2 - n_2')$. This can be used for $\mathcal{F}^{l,n}[\Omega_j p^c]$ as an intermediate step to calculate $\mathcal{F}^{l,n}[\mathfrak{d}_j(\Omega_j p^c)]$. Using these properties, the Fourier transform of the right hand side for the continuous dynamics (4.18) can be constructed.

Discrete Dynamics. Next, we consider the discrete dynamics of the pendulum given by (4.4) and (4.8). The FP equation (3.1b) can be simplified as

$$\frac{\partial p^d(t, R, \tilde{\Omega})}{\partial t} = \int_{\frac{\pi \tilde{\Omega}^-}{L} \in \mathrm{T}^2} \kappa_\Omega(R, \tilde{\Omega}^-, \tilde{\Omega}) \lambda(R, \tilde{\Omega}^-) p^d(t, R, \tilde{\Omega}^-) \mathrm{d}\tilde{\Omega}^- - \lambda(R, \tilde{\Omega}) p^d(t, R, \tilde{\Omega}) \tag{4.22}$$

where $\kappa_\Omega(R^-, \Omega^-, \Omega^+)$ is the second term of the right hand side of (4.8), and $\mathrm{d}\Omega^-$ is the Lebesgue measure on $\mathbb{R}^2$. As the attitude remains unchanged after any collision, the domain of integration in the above expression has been reduced to T^2. More specifically, we have used the property of Dirac-delta function: for any continuous f and $R_0 \in \mathrm{SO}(3)$, $\int_{R \in \mathrm{SO}(3)} \delta(R R_0^T) f(R) \mathrm{d}R = f(R_0)$.

For numerical implementation, the integral in (4.22) can be evaluated with a finite summation using the grid (4.14) on T^2 as in (4.23), where the quadrature weights corresponding to $\mathrm{d}\tilde{\Omega}^-$ is $w'_\mu = \frac{L^2}{(2n_0)^2}$.

$$\begin{aligned} \frac{\partial p^d(t, R_\nu, \tilde{\Omega}_\mu)}{\partial t} \approx & \sum_{\mu_1', \mu_2' = -n_0}^{n_0 - 1} w'_{\mu'} \kappa_\Omega(R_\nu, \tilde{\Omega}^-_{\mu'}, \tilde{\Omega}_\mu) \lambda(R_\nu, \tilde{\Omega}^-_{\mu'}) p^d(t, R_\nu, \tilde{\Omega}^-_{\mu'}) \\ & - \lambda(R_\nu, \tilde{\Omega}_\mu) p^d(t, R_\nu, \tilde{\Omega}_\mu). \end{aligned} \tag{4.23}$$

The density values propagated over the discrete dynamics on the grid can be directly utilized in the subsequent propagation over the continuous dynamics according to the splitting method.

4.4. Simulation Results. The attitude and angular velocity uncertainties of the pendulum model are propagated using Algorithm 3.1, with the explicit computations developed in Section 4.2 and Section 4.3. These are implemented in `c` with Nvidia GPU computing toolkit 11.2, along with a MATLAB interface. The standard FFT on T^N is computed using `cuFFT`,

Table 4.1: Simulation Parameters

Dimensions	h 0.2 m	r 0.025 m	ρ_z 0.1 m	d_{wall} 0.12 m
Inertia	m 1.0642 kg	J_1 0.0144 kg m^2	g 9.8 m s^{-2}	
Cont. Dynamics	$\tilde{B}$ diag(0.2, 0.2) [s^{-1}]	$\tilde{H}_c$ $\begin{bmatrix}1 & 0 & 0\\ 0 & 1 & 0\end{bmatrix}$ [rads$^{-3/2}$]		
Dist. Dynamics	θ_t 5 deg	$\lambda_{\max}$ 100	ε 0.8	H_d diag(0.05, 0.05) [rad s^{-1}]
Computation	l_0, n_0 30	L 14.5 rad s^{-1}	Δt 0.0025 s	

and the discrete convolution in (4.21) and the finite summation in (4.23) are computed using `cuTENSOR` 1.2.2. All of the computations are in double precision. The code is available at [40]. For $l_0 = n_0 = 30$, the computation time of propagating over one time step is 245 seconds in average with a Nvidia A100-40GB GPU.

The initial uncertainty distribution is chosen as follows. The initial attitude follows a matrix Fisher distribution [25] with parameter $F = \exp(-\frac{2\pi}{3}\hat{e}_2)\,\mathrm{diag}(15, 15, 15)$, i.e., the mean attitude is $\exp(-\frac{2\pi}{3}\hat{e}_2)$, and the variance is approximately $\frac{1}{30}\mathrm{rad}^2$ along each axis (Figure 4.3(a)). The initial angular velocity is Gaussian with zero mean and the standard deviation $2\,\mathrm{rad\,s^{-1}}$ (Figure 4.5(a)). The initial attitude and angular velocity are independent. The parameters for the pendulum model and those designed for the computation are listed in Table 4.1. Equation (3.1a) is integrated using the fourth order Runge-Kutta method, and (3.1b) is propagated by the forward Euler's method. The simulation is carried out for eight seconds with the step size of $\Delta t = 0.0025\,\mathrm{s}$.

Propagation of Continuous Dynamics. We first propagate the uncertainty of the pendulum without collisions, i.e., only (3.1a) is integrated. The attitude uncertainty is depicted by the marginal distribution of the coordinates of body-fixed base axes via color shading in Figure 4.3. In other words, the red, greed, and blue shades represent the marginal density of the $\vec{b}_1$, $\vec{b}_2$, and $\vec{b}_3$ axes respectively, and darker color indicates larger density value. Initially, the attitude is concentrated where $\vec{b}_3$ is about 60 deg to the vertical position (Figure 4.3(a)). After the pendulum is released, it swings about the $\vec{e}_2$ axis until it reaches the opposite limit position (Figure 4.3(d)), and swings back to somewhere slightly below the initial position (Figure 4.3(g)), which is repeated later on. At the same time, the uncertainty spreads about the $\vec{b}_3$ axis, i.e., the rotation about $\vec{b}_3$ axis becomes more and more dispersed. After several cycles, the $\vec{b}_3$ axis becomes concentrated near the vertical direction (Figure 4.3(q)-(t)), since the energy is dissipated by the damping of the pendulum. Also, the rotation about $\vec{b}_3$ finally becomes almost uniformly distributed. The same process can be observed from the bottom view for the distribution of $\vec{b}_3$ axis shown in Figure 4.4.

The marginal density for the angular velocity is shown in Figure 4.5. Initially, it is concentrated around zero (Figure 4.5(a)). After the pendulum is released, the angular velocity around $\vec{b}_2$, i.e., Ω_2 accelerates and decelerates in the negative direction (Figure 4.5(b)-(d)), as

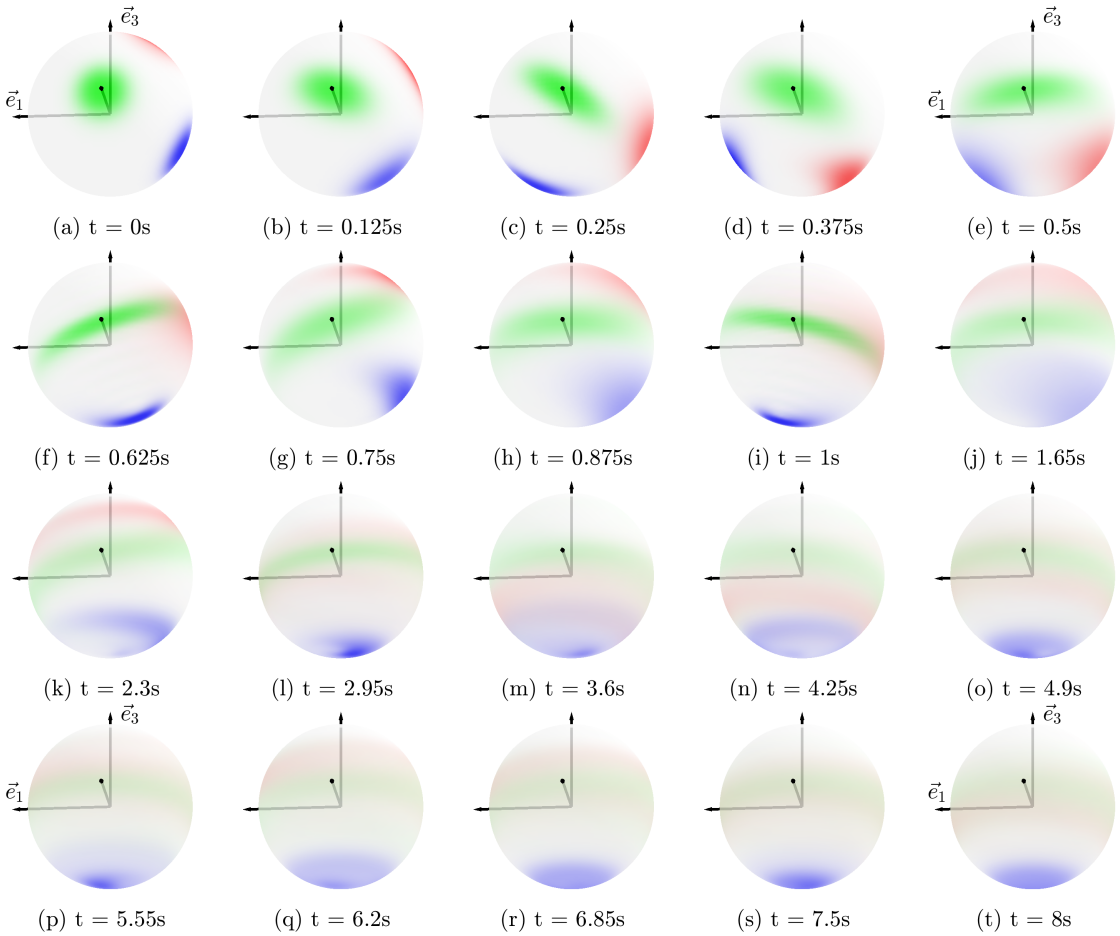

Figure 4.3: Marginal distribution of attitude without collisions.

the pendulum swings and reaches the opposite limit. Then Ω_2 accelerates into the positive direction as the pendulum swings back, and this is repeated. Finally, Ω becomes concentrated near zero again, after the energy is mostly dissipated (Figure 4.5(t)). During the process, the distribution of angular velocity displays some interesting shapes (Figure 4.5(i)-(o)). This is because the area with smaller Ω_1 leads to oscillations compared to other areas with larger Ω_1. This illustrates one of the benefits of the proposed method that is capable of representing an arbitrary density function, and this cannot be achieved with the common Gaussian distribution.

Next, the numerical results of the proposed method are compared against a Monte Carlo simulation with one million samples in Figure 4.6. The differences of the mean attitude and the b_3 direction between the Monte Carlo simulation and the proposed method with $l_0 = n_0 = 20, 30$ are shown in Figure 4.6(a)(b), in terms of angles. It is shown that the difference of the mean direction of $\vec{b}_3$ is below 1.5 deg, which is very small compared to the standard deviation of attitude that is around 15 deg. The difference of the mean attitude

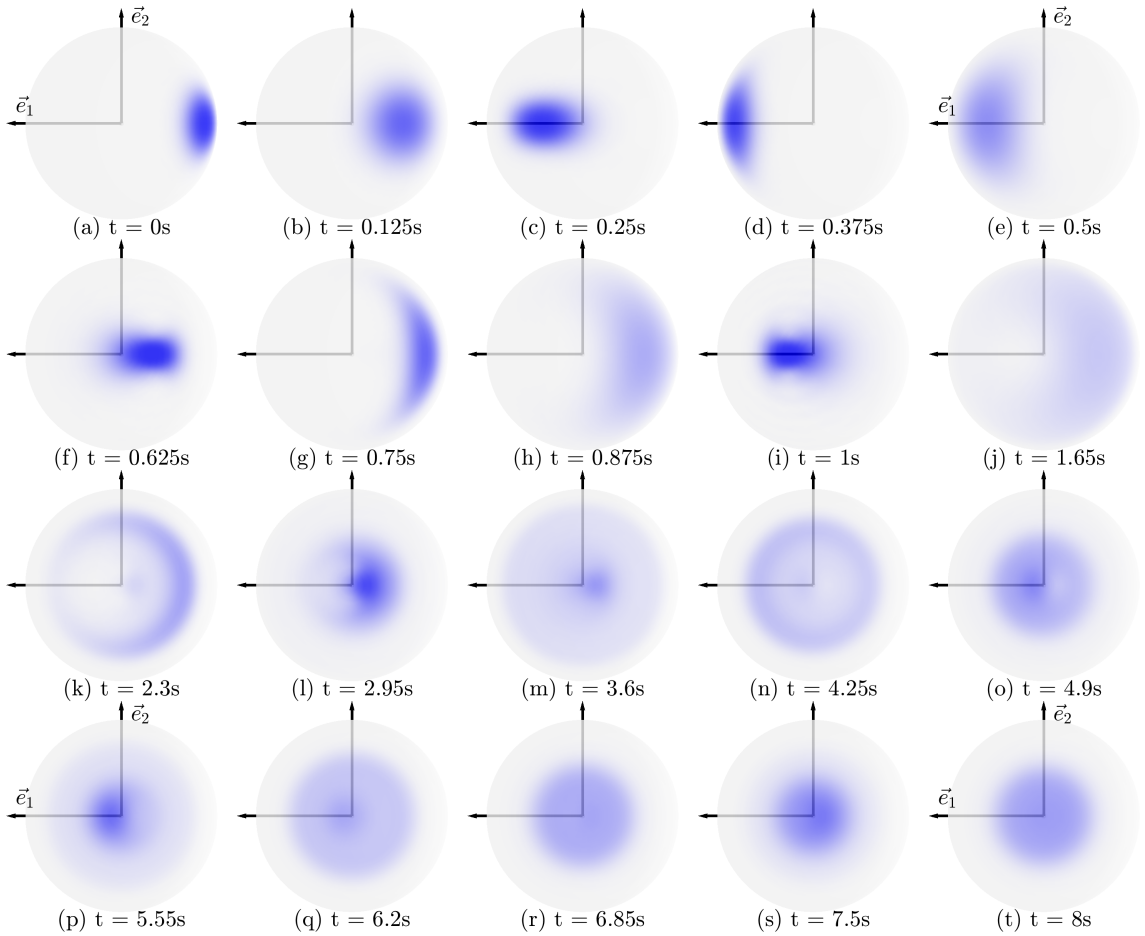

Figure 4.4: Marginal distribution of b_3 without collisions.

becomes relatively large (above 5 deg) after 6 s. However, this is contributed by the fact that the rotation around $\vec{b}_3$ becomes close to a uniform distribution as seen in Figure 4.3(q)-(t), thereby making the mean value less distinctive. The standard deviations of attitude around $\vec{e}_1$ and $\vec{e}_2$ axes are compared in Figure 4.6(c), with their discrepancies more explicitly shown in Figure 4.6(d). Again the differences between the Monte Carlo simulation and the proposed method are small compared to their absolute magnitudes. Similarly, the mean and standard deviation of angular velocity are compared in Figure 4.6(e)(g), with the differences depicted in Figure 4.6(f)(h). In general, the larger bandwidth $b_0 = n_0 = 30$ makes the uncertainty propagation more accurate compared to $b_0 = n_0 = 20$, especially for the dispersion represented by standard deviations. The moments computed by the proposed method are consistent with the Monte Carlo simulation. However, the proposed method provides the probability distribution that carries the complete stochastic properties of the hybrid state beyond the moments.

As another comparison, we also propagate the uncertainty using a Gaussian distribution

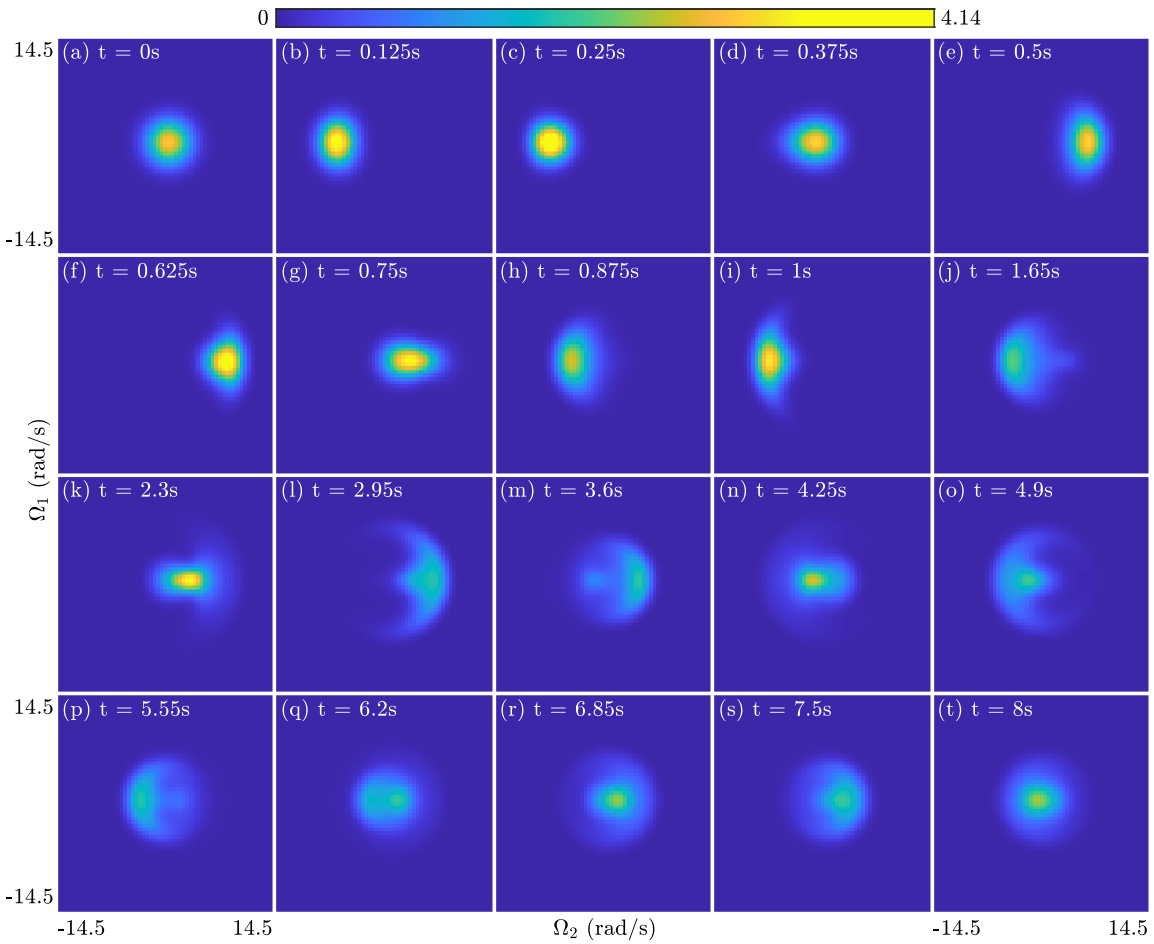

Figure 4.5: Marginal distribution of angular velocity without collisions.

in the tangent space of SO(3) at the nominal attitude. This is the conventional approach when dealing with uncertainties involving 3D attitude. The dynamics in (4.1) is linearized according to [20]. The nominal state, i.e., the mean attitude and angular velocity, is obtained by integrating (4.2) with $\tilde{H}_c = 0$ using the Lie group variational integrator developed in [21] from the initial mean. The covariance matrix is integrated using the 4th order Runge-Kutta method along the standard differential equation obtained through linearization. The comparison of this uncertainty propagation scheme and Monte Carlo simulations is demonstrated in Figure 4.7. Compared to Figure 4.6, the difference is a lot larger than that using the proposed spectral method, rendering the incapability of using a Gaussian distribution in the tangent space of SO(3) for uncertainty propagation of this complex pendulum dynamics. By observing Figure 4.3-Figure 4.5, it is straightforward that Gaussian distribution is deficient in describing the complex shape of the uncertainty.

Propagation of GSHS. Next, we propagate the uncertainty of the pendulum with collisions, i.e., both (3.1a) and (3.1b) are integrated. The marginal distribution of attitude is shown in

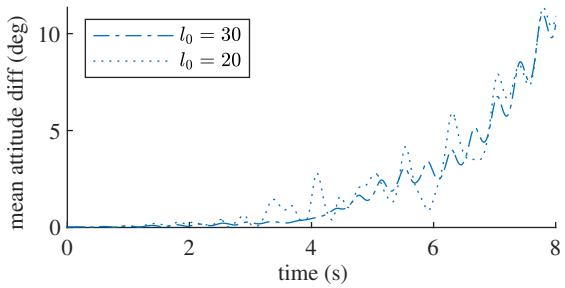

(a) Difference of mean attitude

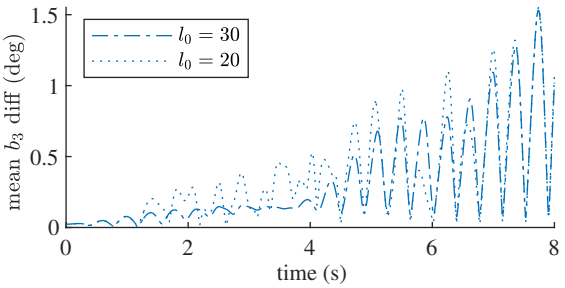

(b) Difference of the mean of b_3

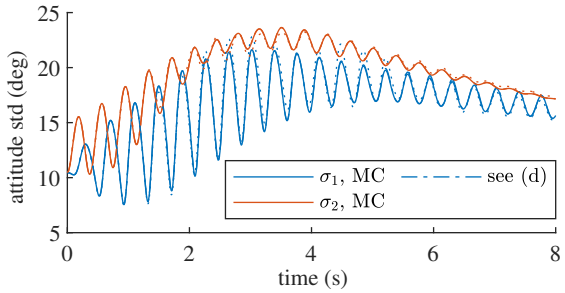

(c) Attitude dispersion

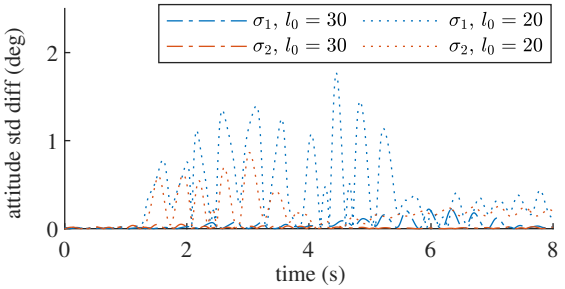

(d) Difference of attitude dispersion

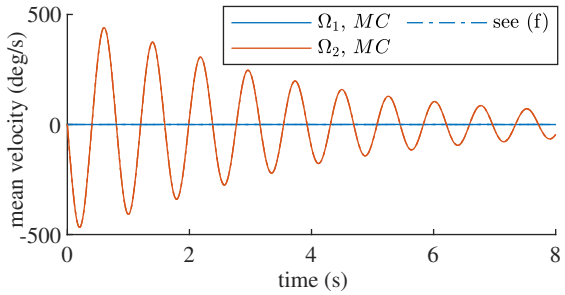

(e) Mean angular velocity

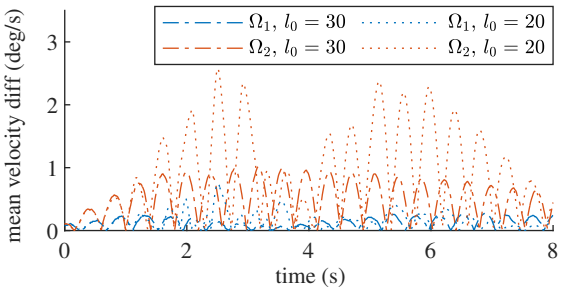

(f) Difference of mean angular velocity

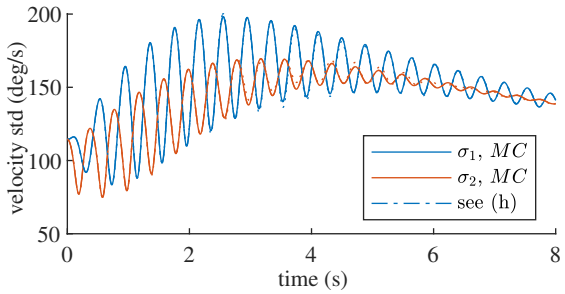

(g) Angular velocity dispersion

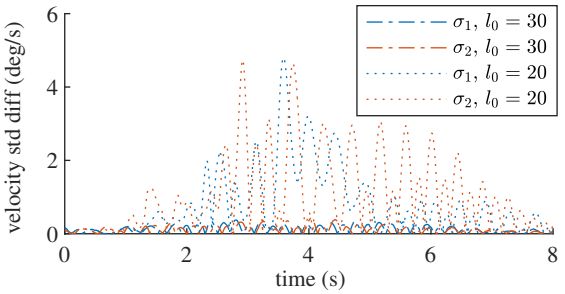

(h) Difference of angular velocity dispersion

Figure 4.6: Comparison of proposed method with Monte Carlo simulation without collisions.

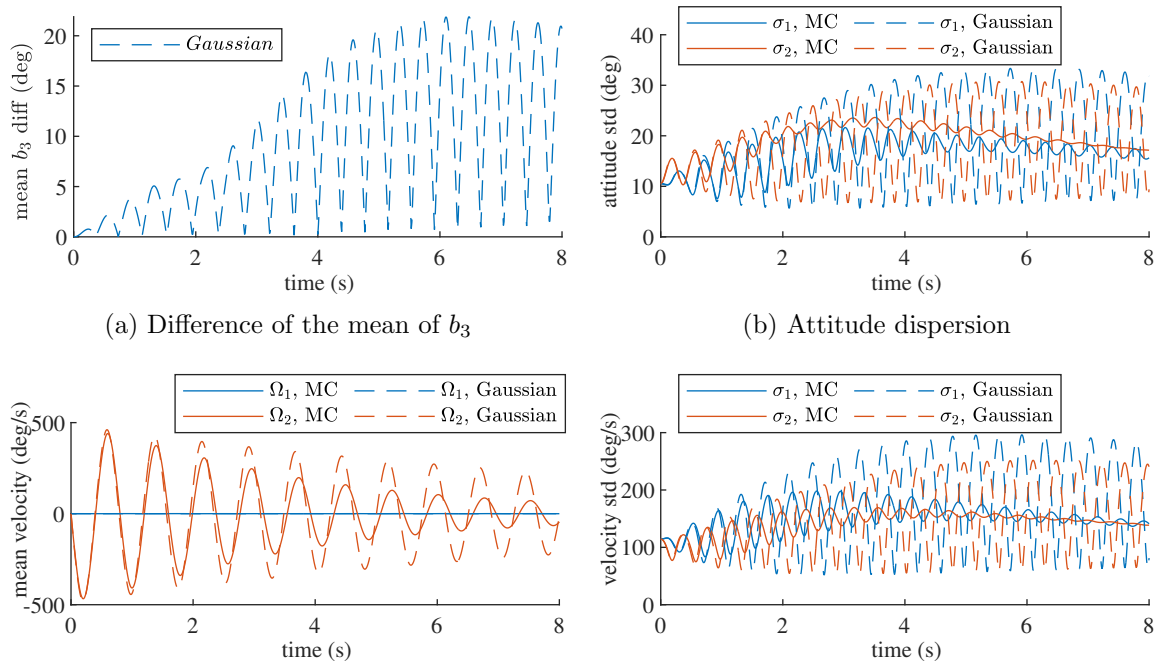

(a) Difference of the mean of b_3

(b) Attitude dispersion

(c) Mean angular velocity

(d) Angular velocity dispersion

Figure 4.7: Comparison of uncertainty propagation using a Gaussian distribution in the tangent space of SO(3) with Monte Carlo simulation without collisions.

Figure 4.8, and in Figure 4.9 where only the marginal distribution of $\vec{b}_3$ is observed from bottom. The wall is depicted by a gray plane. Similar to the case without collisions, initially the attitude is concentrated where $\vec{b}_3$ is 60 deg from the vertical. And after the pendulum is released, it swings about the $\vec{e}_2$ axis. When the pendulum collides with the wall (Figure 4.8(c)), it cannot penetrate through the wall, but rebounds backwards (Figure 4.8(d)). This is more clearly seen by comparing Figure 4.9(c) with Figure 4.4(c). Then the pendulum swings back to somewhere below the initial position (Figure 4.8(e)) due to the friction. These are repeated for several cycles until the energy is mostly dissipated, when $\vec{b}_3$ is concentrated around the vertical direction, and no longer reaches the wall (Figure 4.8(r)-(t)). Compared with the case without collisions, the energy is dissipated more quickly, since it is also lost during the collision due to the coefficient of restitution less than one, besides the damping. Note that there are some densities of b_3 that are slightly on the left of the wall during the collision (Figure 4.9(c),(h)). This is because the rate function (4.4) is not infinitely large in the guard set, thus there is a small probability that the discrete jump is not triggered when the pendulum is on the left. But this probability becomes smaller when the pendulum further penetrates through the wall, since the rate function increases. This can be interpreted as that the probability of rebounds increases as the third body-fixed axis $\vec{b}_3$ becomes closer to the wall. The computational benefit is that the density changes gradually around the boundary of the guard set, instead

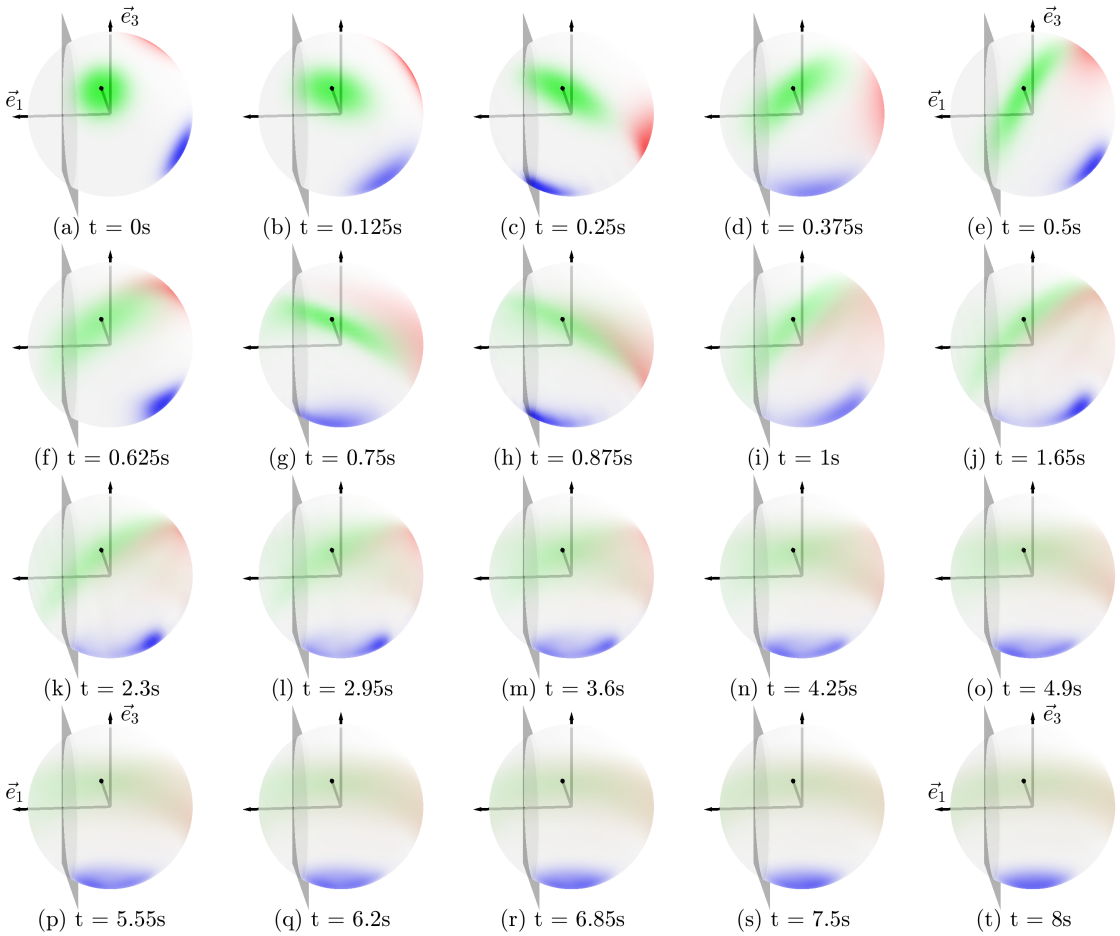

Figure 4.8: Marginal distribution of attitude with collisions.

of becoming zero abruptly like a step function, which allows capturing the space variation of the density function without excessively high bandwidth.

The marginal density of angular velocity is shown in Figure 4.10. Similar to the case without collisions, the angular velocity is concentrated around zero initially (Figure 4.10(a)), and accelerates into the negative Ω_2 direction after the pendulum is released (Figure 4.10(b)). Nevertheless, instead of decelerating to zero, the angular velocity undergoes jump due to the collision, i.e., the negative Ω_2 is reset to be positive instantly during the discrete jump (Figure 4.10(c)) according to the reset kernel (4.8), thereby separating the angular velocity distribution into two parts. Later, most of the angular velocity has completed the collision and Ω_2 continuous to accelerate (Figure 4.10(d)) until the pendulum reaches the vertical position, and begins to decelerate (Figure 4.10(e)) afterwards. These are repeated by several cycles, until the energy is mostly dissipated and the angular velocity is concentrated around zero again (Figure 4.10(r)-(t)). These illustrate that the proposed method successfully captures the complex interplay between the uncertainty distributions of attitude and angular velocity,

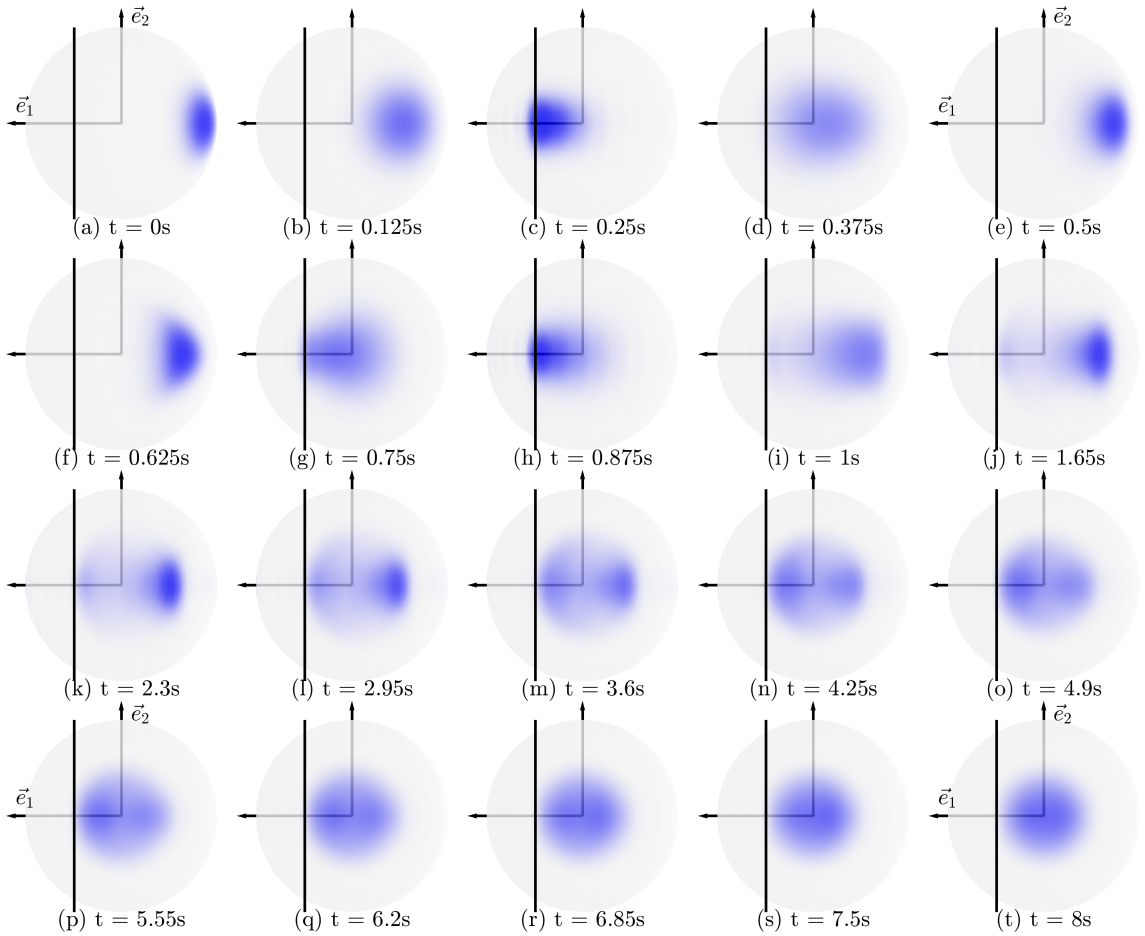

Figure 4.9: Marginal distribution of b_3 with collisions.

as well as the collision, while generating the propagated density function for the hybrid state.

The propagated uncertainty using the proposed method with $l_0 = n_0 = 30$ is also compared with a Monte Carlo simulation with a million samples in Figure 4.11. It is seen the differences of mean attitude and mean direction of $\vec{b}_3$ are small compared with the attitude standard deviation. The differences of attitude standard deviation, mean and standard deviation of angular velocity are in general within 10% of their absolute magnitudes.

5. Conclusions. In this paper, we propose a computational framework to propagate the uncertainty of a general stochastic hybrid system where the continuous state space is a compact Lie group. The Fokker-Planck equation for the GSHS is split into two parts: a partial differential equation corresponding to the continuous dynamics, and an integro-differential equation corresponding to the discrete dynamics. The two split equations are solved alternatively and combined using a first order splitting scheme. In particular, the PDE is solved using the classic spectral method, by invoking noncommutative harmonic analysis on a compact Lie

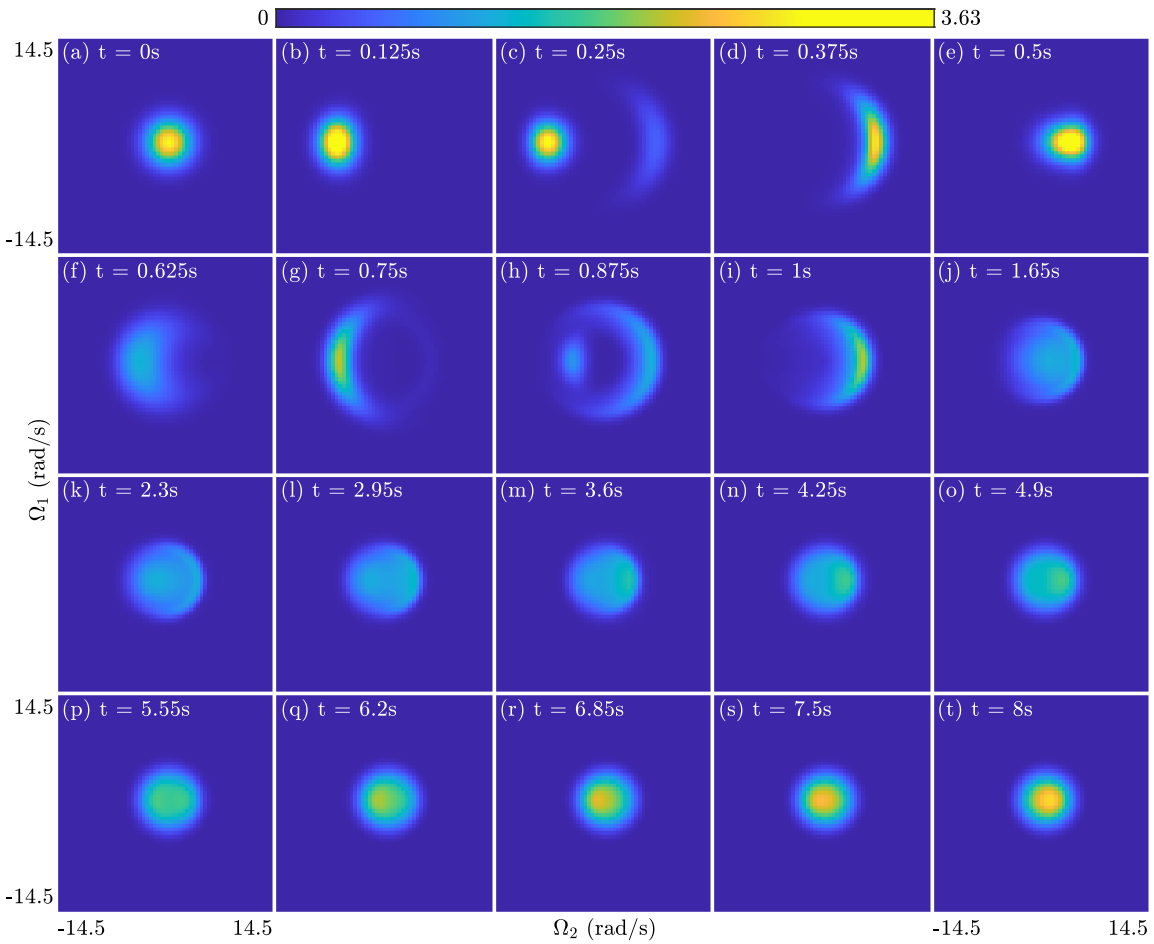

Figure 4.10: Marginal distribution of angular velocity with collisions.

group. The proposed method is applied to a 3D pendulum that collides with a planar wall. It is exhibited that the proposed method is able to capture complex uncertainty distributions with arbitrary shapes or large dispersion, and the computed density function can be directly used for visualization or for constructing any stochastic properties.

REFERENCES

[1] J. Bect, *A unifying formulation of the Fokker–Planck–Kolmogorov equation for general stochastic hybrid systems*, Nonlinear Analysis: Hybrid Systems, 4 (2010), pp. 357–370.

[2] H. A. Blom, G. Bakker, and J. Krystul, *Rare event estimation for a large-scale stochastic hybrid system with air traffic application*, in Rare event simulation using Monte Carlo methods, Wiley Online Library, 2009, ch. 9, pp. 193–214.

[3] H. A. Blom and Y. Bar-Shalom, *The interacting multiple model algorithm for systems with Markovian switching coefficients*, IEEE transactions on Automatic Control, 33 (1988), pp. 780–783.

[4] H. A. Blom and E. A. Bloem, *Particle filtering for stochastic hybrid systems*, in IEEE Conference on

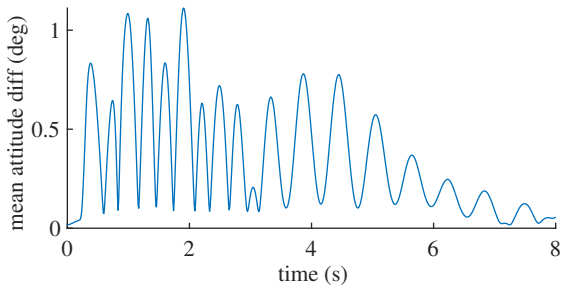

(a) Difference of mean attitude

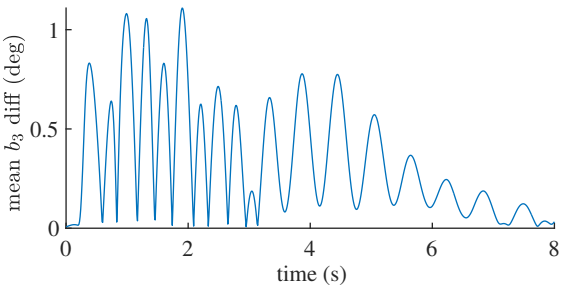

(b) Difference of the mean of b_3

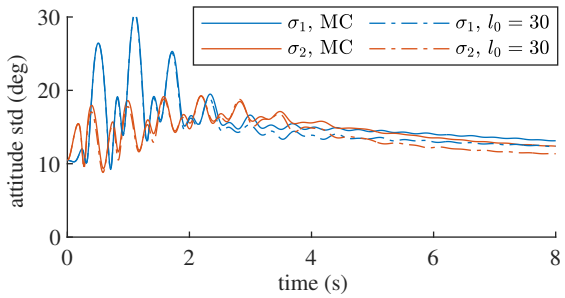

(c) Attitude dispersion

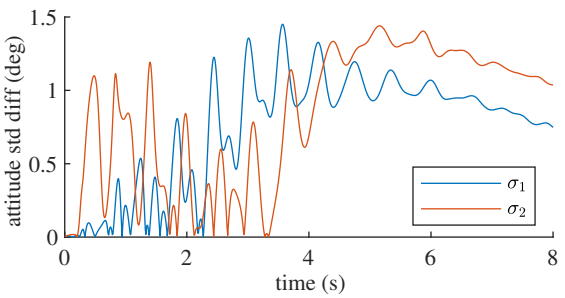

(d) Difference of attitude dispersion

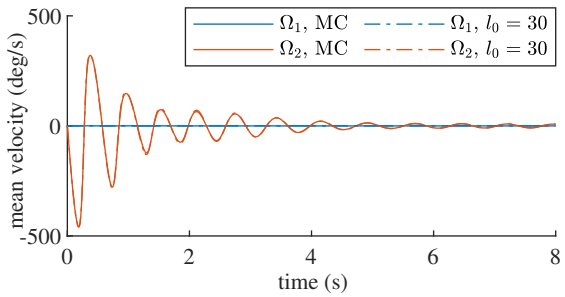

(e) Mean angular velocity

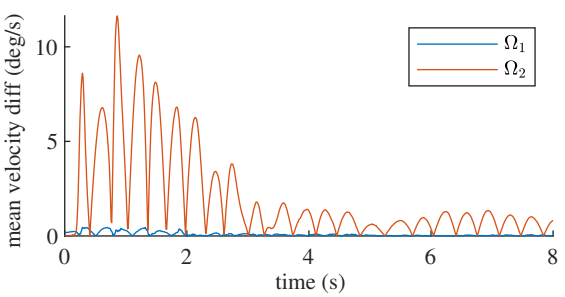

(f) Difference of mean angular velocity

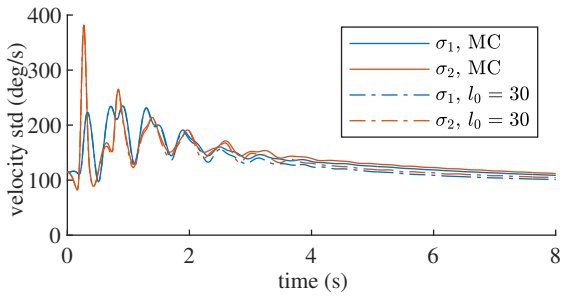

(g) Angular velocity dispersion

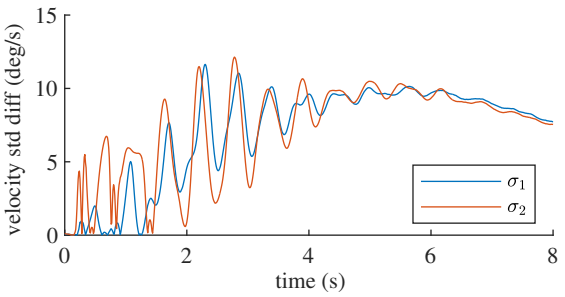

(h) Difference of angular velocity dispersion

Figure 4.11: Comparison of proposed method with Monte Carlo simulation with collisions.

Decision and Control, IEEE, 2004, pp. 3221–3226.
[5] M. L. Bujorianu and J. Lygeros, *Toward a general theory of stochastic hybrid systems*, in Stochastic hybrid systems, Springer, 2006, pp. 3–30.
[6] G. Chirikjian and M. Kobilarov, *Gaussian approximation of non-linear measurement models on Lie groups*, in 53rd IEEE Conference on Decision and Control, IEEE, 2014, pp. 6401–6406.
[7] G. S. Chirikjian, *Stochastic models, information theory, and Lie groups, volume 2: Analytic methods and modern applications*, vol. 2, Springer Science & Business Media, 2011.
[8] G. S. Chirikjian and A. B. Kyatkin, *Engineering applications of noncommutative harmonic analysis: with emphasis on rotation and motion groups*, CRC press, 2000.
[9] H. Dong and G. S. Chirikjian, *A comparison of Gaussian and Fourier methods for degenerate diffusions on* SE(2), in 2015 54th IEEE Conference on Decision and Control, IEEE, 2015, pp. 6016–6022.
[10] J. Hammersley and D. Handscomb, *Monte Carlo methods*, Methuen, 1975.
[11] J. P. Hespanha, *Stochastic hybrid systems: Application to communication networks*, in International Workshop on Hybrid Systems: Computation and Control, Springer, 2004, pp. 387–401.
[12] J. P. Hespanha and A. Singh, *Stochastic models for chemically reacting systems using polynomial stochastic hybrid systems*, International Journal of Robust and Nonlinear Control, 15 (2005), pp. 669–689.
[13] R. Iyengar and P. Dash, *Study of the random vibration of nonlinear systems by the Gaussian closure technique*, Journal of Applied Mechanics, 45 (1978), pp. 393–399.
[14] J. S. Kim and G. S. Chirikjian, *Bayesian filtering for orientational distributions: A Fourier approach*, in 18th International Conference on Information Fusion, IEEE, 2015, pp. 748–753.
[15] N. J. Kong, J. J. Payne, G. Council, and A. M. Johnson, *The salted Kalman filter: Kalman filtering on hybrid dynamical systems*, Automatica, 131 (2021), p. 109752.
[16] P. J. Kostelec and D. N. Rockmore, *FFTs on the rotation group*, Journal of Fourier analysis and applications, 14 (2008), pp. 145–179.
[17] M. Kumar, P. Singla, S. Chakravorty, and J. Junkins, *The partition of unitiy finite element approach to the stationary Fokker-Planck equation*, in AIAA/AAS Astrodynamics Specialist Conference and Exhibit, 2006.
[18] T. Lee, *Stochastic optimal motion planning for the attitude kinematics of a rigid body with non-Gaussian uncertainties*, Journal of Dynamic Systems, Measurement, and Control, 137 (2015), p. 034502.
[19] T. Lee, M. Leok, and N. H. McClamroch, *Global symplectic uncertainty propagation on* SO(3), in 47th IEEE Conference on Decision and Control, IEEE, 2008, pp. 61–66.
[20] T. Lee, M. Leok, and N. H. McClamroch, *Stable manifolds of saddle points for pendulum dynamics on* $\mathbb{S}^2$ *and* SO(3), arXiv preprint arXiv:1103.2822, (2011).
[21] T. Lee, N. H. McClamroch, and M. Leok, *A Lie group variational integrator for the attitude dynamics of a rigid body with applications to the 3D pendulum*, in Proceedings of IEEE Conference on Control Applications, IEEE, 2005, pp. 962–967.
[22] C. Levermore and W. Morokoff, *The Gaussian moment closure for gas dynamics*, SIAM Journal of Applied Mathematics, 59 (1998), pp. 72–96.
[23] W. Liu and I. Hwang, *On hybrid state estimation for stochastic hybrid systems*, IEEE Transactions on Automatic Control, 59 (2014), pp. 2615–2628.
[24] S. MacNamara and G. Strang, *Operator splitting*, in Splitting methods in communication, imaging, science, and engineering, Springer, 2016, pp. 95–114.
[25] K. V. Mardia and P. E. Jupp, *Directional statistics*, vol. 494, John Wiley & Sons, 2009.
[26] D. K. Maslen, *Efficient computation of Fourier transforms on compact groups*, Journal of Fourier Analysis and Applications, 4 (1998), pp. 19–52.
[27] N. Metropolis and S. Ulam, *The Monte Carlo method*, Journal of the American Statistical Association, 44 (1949), pp. 335–341.
[28] K. Pakdaman, M. Thieullen, and G. Wainrib, *Fluid limit theorems for stochastic hybrid systems with application to neuron models*, Advances in Applied Probability, 42 (2010), pp. 761–794.
[29] F. Peter and H. Weyl, *Die vollständigkeit der primitiven darstellungen einer geschlossenen kontinuierlichen gruppe*, Mathematische Annalen, 97 (1927), pp. 735–755.
[30] H. Pradwarter, *Nonlinear stochastic response distribution by local statistical linearization*, International Journal of Nonlinear Mechanics, 36 (2001), pp. 1135–1151.

[31] M. Prandini and J. Hu, *Application of reachability analysis for stochastic hybrid systems to aircraft conflict prediction*, in 47th IEEE Conference on Decision and Control, IEEE, 2008, pp. 4036–4041.
[32] J. Roberts and P. Spanos, *Random vibration and statistical linearization*, Dover Publications, 2003.
[33] D. N. Rockmore, *Recent progress and applications in group FFTs*, in Computational noncommutative algebra and applications, Springer, 2004, pp. 227–254.
[34] C. E. Seah and I. Hwang, *Stochastic linear hybrid systems: modeling, estimation, and application in air traffic control*, IEEE Transactions on Control Systems Technology, 17 (2009), pp. 563–575.
[35] E. Tadmor, *A review of numerical methods for nonlinear partial differential equations*, Bulletin of the American Mathematical Society, 49 (2012), pp. 507–554.
[36] S. Tafazoli and X. Sun, *Hybrid system state tracking and fault detection using particle filters*, IEEE Transactions on Control Systems Technology, 14 (2006), pp. 1078–1087.
[37] D. A. Varshalovich, A. N. Moskalev, and V. K. Khersonskii, *Quantum theory of angular momentum*, World Scientific, 1988.
[38] W. Wang and T. Lee, *Spectral Bayesian estimation for general stochastic hybrid systems*, Automatica, 117 (2020), p. 108989.
[39] W. Wang and T. Lee, *Spectral uncertainty propagation for generalized stochastic hybrid systems with applications to a bouncing ball*, in American Control Conference, IEEE, 2020, pp. 1803–1808.
[40] W. Wang and T. Lee, *Uncertainty propagation for GSHS*. [Online]. Available: https://github.com/fdcl-gwu/hybrid_UP, 2021.
[41] Y. Wang, Y. Zhou, D. K. Maslen, and G. S. Chirikjian, *Solving phase-noise Fokker-Planck equations using the motion-group Fourier transform*, IEEE Transactions on Communications, 54 (2006), pp. 868–877.
[42] Y. Zhou and G. S. Chirikjian, *Probabilistic models of dead-reckoning error in nonholonomic mobile robots*, in 2003 IEEE International Conference on Robotics and Automation, vol. 2, IEEE, 2003, pp. 1594–1599.